Interferometric Scheme for High-Sensitivity Coaxial Focusing in Projection Lithography

Chengliang Di
Song Hu
Wei Yan
Yanli Li
Guang Li
Junmin Tong
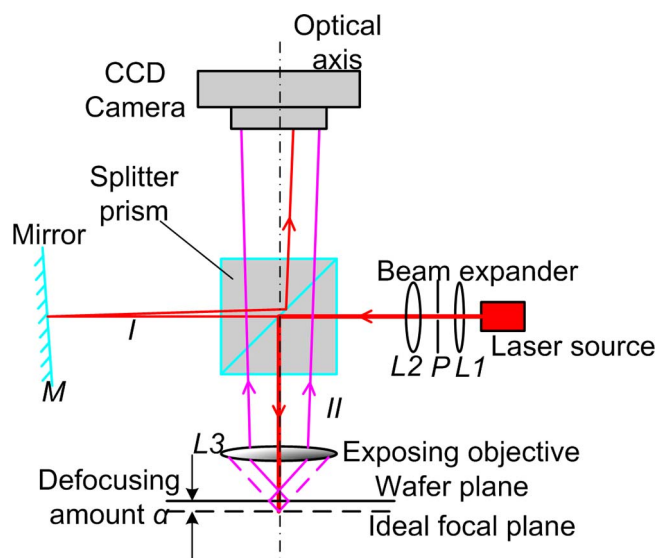
Interferometric Scheme for High-Sensitivity Coaxial Focusing in Projection Lithography

Chengliang Di,[1,2] **Song Hu,**[1] **Wei Yan,**[1] **Yanli Li,**[1]
Guang Li,[1,2] **and Junmin Tong**[3]

[1]State Key Laboratory of Optical Technologies for Microfabrication, Institute of Optics and Electronics,
Chinese Academy of Sciences, Chengdu 610209, China
[2]University of Chinese Academy of Sciences, Beijing 100049, China
[3]Xuchang Vocational and Technical College, Xuchang 461000, China

Abstract: Focusing of wafer plane is an essential factor to determine the ultimate feature size of the stepper such as projection lithographic system. Based on Michelson interferometeric system, this paper demonstrates an interferometric focusing scheme for projection lithography to coaxially locate the ideal focal plane of the projective objective. The collimated incident laser beam is divided into the reference arm and object arm. The latter propagates through the objective lens and then interferes with the slightly deflected reference beam that reflected back by a fixed mirror, giving rise to an interferential pattern on the CCD. Any amounts of defocusing can be directly indicated from the demodulated phase of the interferential pattern. In this manner, the focusing sensitivity at nanometer scale is experimentally attainable, which shows great superiority over traditional methods, particularly the limited focal length of current projective objective lens.

Index Terms: Interferometry, metrology, fringe analysis, phase unwrapping, lithography.

1. Introduction

Focusing, which is an imperative step to locate the ideal focal plane to ensure the uniformity of critical dimension of final micro/nano structures, has been an essential process during projection lithography, particularly when the depth of focus (DOF) of projective objective lens shrink drastically caused by improved resolution [1], [2].

Traditionally, the focusing process was performed by construction of a triangular optical path with the reflected beam from wafer surface to transform the up and down fluctuation of the horizontally placed wafer plane into displacement of reflected light spot on the photo-detector. To adapt the demand of focusing with relatively low accuracy, a bar or slot like geometric mark was used as a moving reference to determine the vertical position of the wafer by imaging the mark onto a detector [3], [4]. To further improve the accuracy of these geometric imaging methods, other methods of optical homodyne [5], [6] or heterodyne interferometry [7] emerged to measure the vertical position or offset of wafer by detecting the intensity or phase of interfered beams. In addition, there also appeared a real-time *in situ* wafer monitoring system that combined with two interference sub-systems and a focus monitoring sub-system [8]. The interferential sub-systems were utilized to measure the warpage and distortion of the entire exposing filed, and the focus monitoring sub-system was
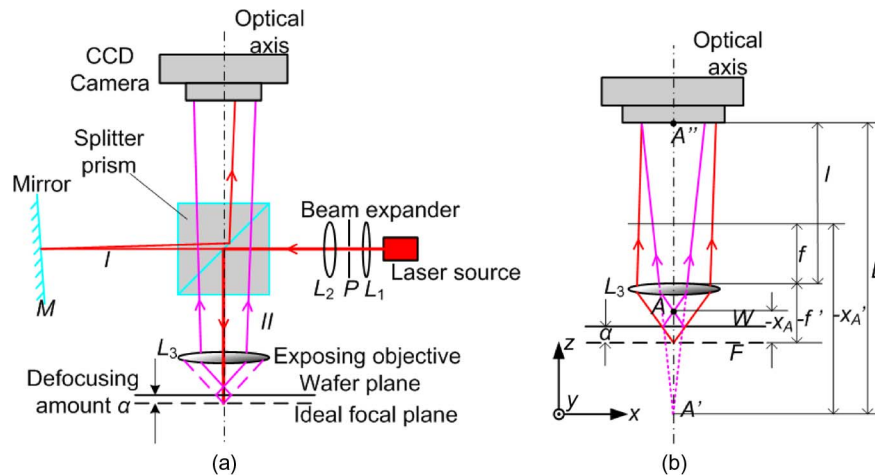
Fig. 1. (a) Schematic diagram of the coaxial focusing setup. (b) A detailed schematic with mathematics marks.

conducted to determine the best focus. More recently, the moiré techniques were used by employing series of moiré fringes generated by two gratings with close periods to realize nanometer level measurement [9]–[12]. However, all those techniques mentioned above measure and adjust the vertical position of the wafer with regard to the projective objective lens in an "Off-axis" way, i.e., the off-axis focusing, in which the ideal focal plane is indirectly determined by comparing the current wafer position to a pre-defined ideal focus position. Particularly, higher resolution of the projective lithographic system leads to smaller distance between the wafer and objective, as well as more challenges that emerge to install and debug those complicated triangular focusing schemes.

Alternatively, this paper firstly proposes a coaxially interferometric focusing method based on a modified Michelson-interferometer. Any amounts of defocusing are directly demodulated from the phase distribution of the interferential patterns formed by the reference beam and object beam. This focusing scheme can be performed in such a coaxial or on-line way that the collimated object beam penetrates the projective objective lens back and forth after reflection by the wafer surface. This method also tends to be unaffected by the tiny gap between wafer and objective with great potential to be applied in the immersion lithography, which limits the application of traditional "Off-axis" techniques due to the existence of fluid between objective lens and wafer [13], [14].

2. Principle

The principle of this coaxially interferometric focusing method can be explained by referring to Fig. 1(a). Two lenses (L_1 and L_2) and a pinhole filter, located at the front focus of L_1 and the back focus of L_2, are used to constitute a beam expander. A monochromic planar wave is produced by filtering and collimating the beam emitted by a HE-NE laser source. At the incidence, this monochromic planar wave with wavelength λ is divided into two beams by a splitter prism, i.e., the reference beam (I) and object beam (II) to construct an interferometer in Fig. 1. On the one hand, the beam (I) on the reference arm is reflected back and deviated from the horizontal direction by a fixed mirror (M) that is perpendicular with the xoz plane but slightly deflected with regard to the z-axis. Then the back reflected reference beam (I) directly reach the image plane of CCD camera after deflection again by the splitter prism. In the surface plane of the CCD, the complex amplitude of beam I can be readily expressed as

$$E_1(x, y) = C\exp(jkKx)\exp(jkZ) \qquad (1)$$

where C is the amplitude of Beam I; and k is the wave vector; and K is the obliquity factor of mirror K; and z is the coordinate of CCD image plane at the Z axis.

On the other hand, the object beam *II* is directed by the splitter to vertically propagate through the objective lens to arrive at the wafer surface, which reflects the object beam back to coaxially travel through the projective lens again to finally interfere with the reference beam *I* on the CCD image plane. When the wafer surface is horizontally located at the ideal focal plane of the objective lens, the back reflected object beam *II* turns out to be a planar wave so that interference of two beams produces a spatially varied one-dimension intensity distribution, i.e., a set of linear fringes recorded by CCD.

Taking into account any amount of defocusing α, by which when the wafer plane is actually deviated from the ideal focal plane and the wave front of back reflected object beam *II* turns into spherical, the complex amplitude of beam *II* can be readily expressed as

$$E_2(x, y) = B\exp(jk(r - L)) + \varphi(0, 0)) \tag{2}$$

where B is the amplitude of Beam *II*, and $r = \sqrt{L^2 + x^2 + y^2}$, and $L = l + x'_a - f'$ is the distance between the point A and the CCD plane, shown in Fig. 1(b). Meanwhile, $\varphi(0, 0)$ is the constant phase of point A'' and can be expressed as

$$\varphi(0, 0) = \exp(jk(l + f - 2\alpha)). \tag{3}$$

In order to explicitly reveal the relationship between the defocusing amount α and the amplitude of Beam *II*, $E_2(x, y)$ is derived and rewritten as

$$E_2(x, y) = B\exp(jk(l + f - 2\alpha)) \cdot \exp\left(jk\frac{x^2 + y^2}{2(l - f') + \frac{-f \cdot f'}{\alpha}} \right). \tag{4}$$

Finally, the beam *I* interferes with beam *II* at the CCD image plane. The interferential fringes are then two-dimensionally deformed in accordance with the phase variation as well as the amount of defocusing. Their intensity field can thus be derived as

$$I(x, y) = (E_1 + E_2) \cdot (E_1 + E_2)^* = C'^2 + B'^2 + 2B'C'\cos\left(k\frac{x^2 + y^2}{2(l - f') + \frac{-f \cdot f'}{\alpha}} - 2k\alpha - kKx \right). \tag{5}$$

Obviously, the amount of defocusing of wafer with regard to the objective lens is encoded into phase distribution of the intensity field in such a way that any positive or negative value of α cause a spherically distorted phase in Eq. (6), shown below, and horizontal migrated phase Eq. (7), also shown below:

$$\varphi_{spherical} = k\frac{x^2 + y^2}{2(l - f') + \frac{-f \cdot f'}{\alpha}} \tag{6}$$

$$\varphi_{horizontal} = 2k\alpha. \tag{7}$$

Applying a phase unwrapping algorithm on the interferential fringes, a phase map can be extracted. At every pixel point (x, y) a defocusing amount $\alpha_{(x,y)}$ could be figured out through Eq. (6). And an average $\alpha_{(x,y)}$ value of all pixels can better express a more precise result.

3. Simulation

To confirm the validity of this scheme, the interferential fringe patterns with corresponding phase distributions are simulated according to the associated defocusing amount. The simulated results with both negative and positive defocusing are, respectively demonstrated in the form of phase distributions as well as corresponding fringes patterns, as shown in Fig. 2.

The defocusing amounts turn out to be directly in agreement with the phase distribution of corresponding fringe patterns. When the defocusing amount is set to be $-40\ \mu$m, prominent spherical phase distortion attains to be observable, see the deep bowl phase distribution which exactly describes the eccentric fringes pattern as shown in Fig. 2(a) and (e). As the defocusing
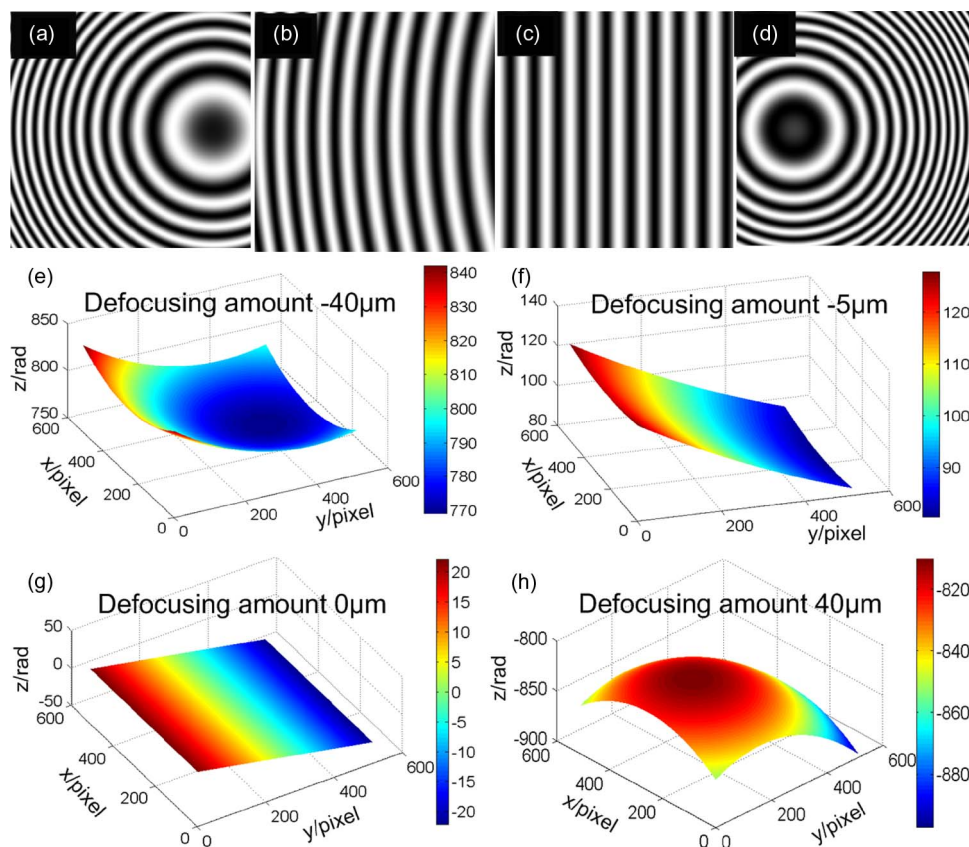
Fig. 2. Simulated phase distributions and corresponding patterns with different defocusing amounts for (a) and (e) −40 μm, (b) and (f) −5 μm, (c) and (g) 0 μm, (d) and (h) 40 μm.

amount decreases to −5 μm, the slowly varied phase distribution with a concave slope [Fig. 2(f)] shows the curve fringes in Fig. 2(b). The one dimensionally periodic fringes can be observed [Fig. 2(c)] when the wafer plane is adjusted to be overlapped with the ideal focal plane (Defocusing amount = 0 μm). Under such a condition, the phase distribution appears to be linearly varied, i.e., a plane [Fig. 2(g)] with constant slope. Furthermore, a positive 40 μm defocusing amount shows a convex deep bowl phase distribution of which the center area has migrated towards the left side of the pattern as shown in Fig. 2(d) and (h). In summary, a specific defocusing amount corresponds to a unique phase distribution.

According to Eq. (5) and Fig. 2(b), if the defocusing amount is relatively small, the fringes can be treated approximately as straight fringes. Applying 2-Dimension Fourier transform on the inter-ferential pattern, its phase map can be detected with a fundamental frequency K/λ [15], [16]. As the defocusing amount increases, there is a drastic increase in the curvature of interferential pattern, for instance the annular fringes emerge in Fig. 2(a) and (d). Obviously, the bending direction and the frequencies of the fringes vary on almost continuously throughout the whole fringe pattern which would lead to frequency spectrum aliasing by Fourier transform. Alternatively, we can choose a Wavelet transform with great superiorities to demodulate the phase of circular interferential pattern [17], [18].

When used in a real system, the interferential patterns are affected by the disturbances from light fluctuation, imaging system or environmental factors. The disturbances alter the high frequency in interferential fringes; however, turning the smoothly phase distributions into undulated rough topography. To investigate the robustness of phase unwrapping algorithms, we add Gaussian noise with different SNR (Signal to noise ratio) to Fig. 2(a)–(d), as shown in Fig. 3. Demodulating the phase distributions of those noise-polluted fringes in Fig. 3, focusing errors are obtained according
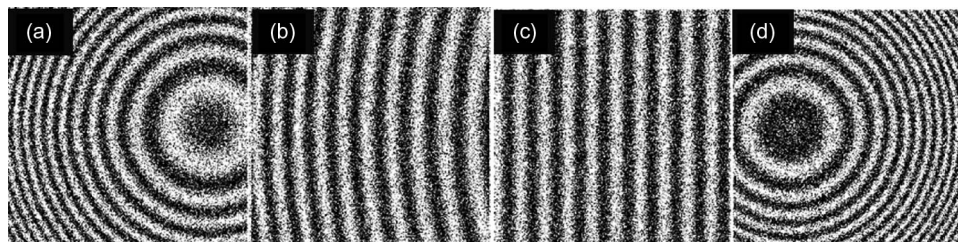
Fig. 3. Interferential fringe patterns polluted by Gaussian noise with 0.2 variance.

TABLE 1

Focusing errors calculated from noise-polluted patterns with different defocusing amounts

Variations of noise	errors in Fig. 3(a)	errors in Fig. 3(b)	errors in Fig. 3(c)	errors in Fig. 3(d)
0.1	$0.352\mu m$	$0.020\mu m$,	$0.003\mu m$	$0.395\mu m$
0.2	$0.413\mu m$	$0.025\mu m$,	$0.002\mu m$	$0.440\mu m$
0.3	$0.500\mu m$	$0.027\mu m$,	$0.004\mu m$	$0.492\mu m$

to Eq. (5) and Eq. (6) and tabulated in Table 1. Statistics in Table 1 indicate that the Fourier or Wavelet based algorithms are competent to precisely demodulate the interferential patterns. However, the focusing errors of Fig. 3(a) and (d) are slightly larger than that of Fig. 3(b) and (c). This is because that the periods of fringes in Fig. 3(a) and (d) vary much drastic than that in Fig. 3(b) and (c), and the high-frequency fringes in the border of Fig. 3(a) and (d) are more sensitive to the disturbances.

4. Experimental Results and Discussions

Including the defocusing amount extraction and wafer adjustment, the focusing of wafer plane generally acts as a close-loop feedback model. To achieve a perfect focusing, two interdependent steps should be followed, i.e., first, the defocusing amount is measured by demodulating the phase distribution of the interferential patterns captured by CCD; second, a mechanical servo diver and/or a piezoelectric servo motor adjust the position of the wafer according to the defocusing amount. These two steps always work simultaneously in real-time; and perfect wafer focusing could be accomplished until the defocusing amount is smaller than a pre-defined threshold, e.g., 10 nm.

To experimentally confirm this interferometric focusing scheme in a proof-of-concept way, we construct an experimental setup (shown in Fig. 4) according to the diagram in Fig. 1. The defocusing amount extraction mentioned in the first step is demonstrated, instead of the whole close-loop focusing model. The final accuracy performance will be calibrated by referring to the high-precision dual-frequency laser interferometer.

In experiment, a focusing illumination source with 632.8 nm wavelength and 5 mW output power, along with collimating lens provide a uniform and collimated planar light. And the obliquity factor K of mirror is set to be about 0.001 rad, while the focal length of projective objective is 2900 μm. Under the wafer, a piezoelectric translator (PZT, the resolution and stroke are, respectively 2 nm (closed loop) and 200 μm) is adopted to perform the step movement of wafer. At the same time, a dual-frequency laser interferometer (Renishaw XL/80, with a linear resolution of 1 nm) monitors the defocusing amount in real time. The interferential patterns are captured by a CCD (WAT902H2, China. 768 $\times$ 576) with pixel width of about 10 μm. The captured interferential fringes are processed using 2-Dimensional phase unwrapping algorithm to obtain the defocusing amounts. In experimental setup, whole system is carefully adjusted to achieve uniform illumination and clearly interferential patterns on the CCD imaging system.
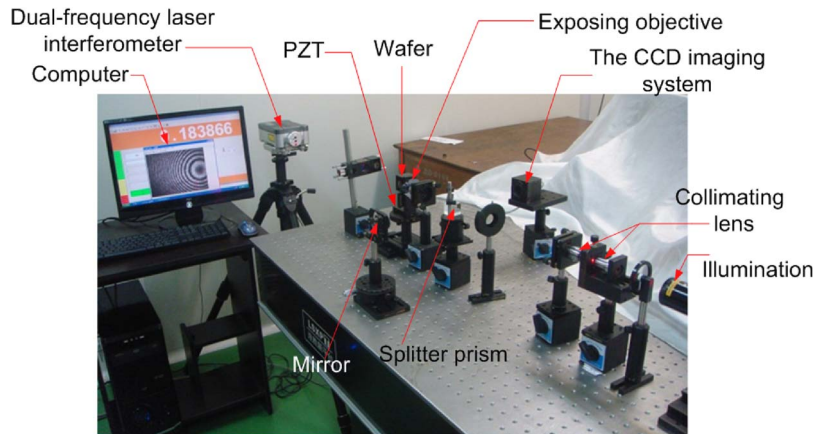
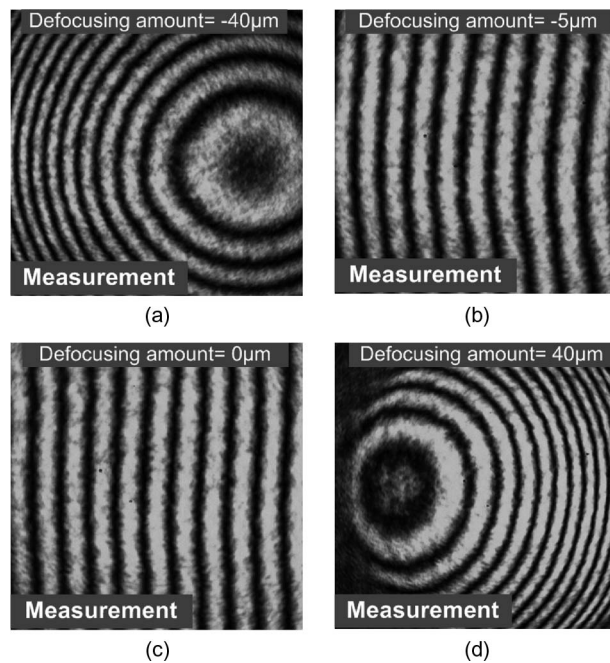Fig. 4. The experimental setup conducted according to the schematic in Fig. 1.

Fig. 5. Measured interferential patterns with different defocusing amounts. (a) -40 μm, (b) -5 μm, (c) 0 μm, and (d) 40 μm.

With the assistance of PZT at different step lengths, series of experimental results are captured with different defocusing amounts. For the sake of comparison, fringe patterns are shown at those locations with the same defocusing amounts as counterparts in Fig. 2.

Apparently, the distributions of the captured fringe patterns in Fig. 5 are in good agreement with those simulated results in Fig. 2, which directly proves our theoretical ratiocination. Fig. 5(a), (b), and (d) indicate that the decreased absolute value of defocusing amount can be directly monitored by the decreased curvature of the fringes pattern too.

By comparing the straightness (or curvature) of the interferential fringes in Figs. 5(c) and 2(c), it evidently shows that the projective objective L_3 is not aberration-free due to some deformed fringes. Since the focusing and defocusing points A and A' are both optical on-axis, we could feasibly suppose that the patterns suffer mainly from spherical aberration which is closely associated with
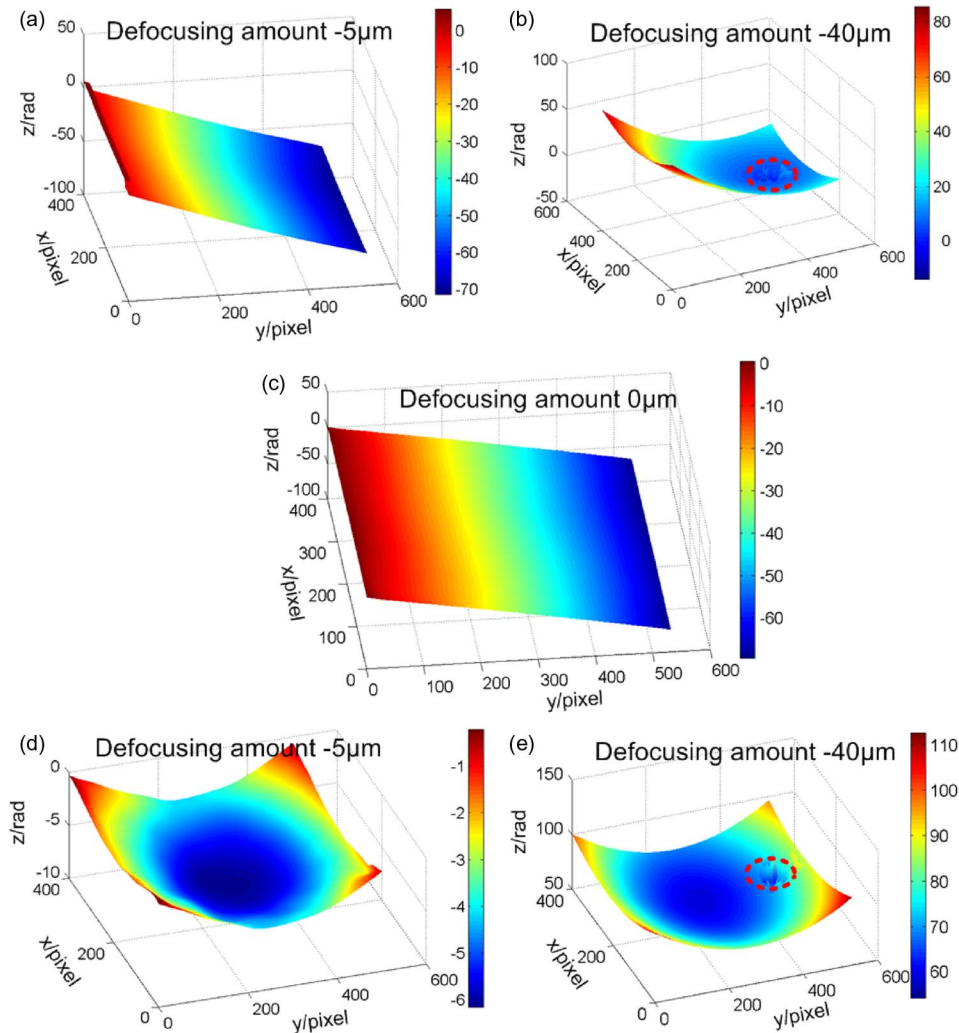
Fig. 6. (a) Phase distribution with -5 μm defocusing amount. (b) Phase distribution with -40 μm defocusing amount. (c) Phase distribution with 0 μm defocusing amount. (d) Phase difference between (a) and (c). (e) Phase difference between (b) and (c).

the aperture of reflected beam II from the wafer. When the wafer is defocused away from the ideal focal plane, the aperture has a tiny but negligible variation and can be regarded as a constant, which means that spherical aberration has almost the same amount of influence on fringes with different defocusing amounts. Therefore, to avoid the negative impact caused by the aberration, we compensate that by subtracting a reference phase distribution (usually the pattern with 0 μm defocusing amount) from that of the designated fringe pattern with defocusing amount α.

Fig. 6(a) and (b) are phase distributions extracted from Fig. 5(b) and (a), respectively. Subtracting the reference phase distribution (with 0 μm defocusing amount as shown in Fig. 6(c)) from the original ones in Fig. 6(a) and (b), two spherical phase distributions are present in Fig. 6(d) and (e) as expectedly according to Eq. (5). Apart from the spectrum aliasing (The red circles in Fig. 6(b) and (e)), phase distributions in Fig. 6(d) and (e) manifest a good concentricity. By working backward from the spherical phase distributions, defocusing amounts are figured as -4.952 μm and -40.632 μm with errors 0.048 μm and -0.632 μm, respectively.

Furthermore, to verify the feasibility of the aberration compensation method and the accuracy of the coaxial focusing scheme, the calculated focusing errors are plotted in Fig. 7 by comparing the reference defocusing amounts that are measured by the dual-frequency laser interferometer. The
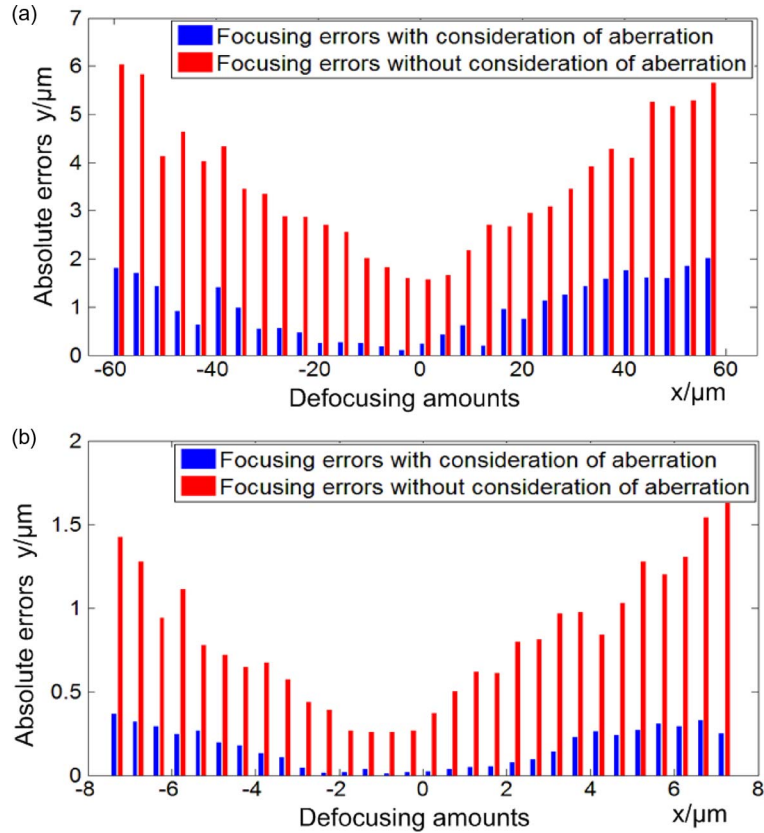
Fig. 7. Absolute focusing errors that calculated with/without consideration of the objective aberration. (a) The step length of PZT is set to be 4 μm. (b) The step length of PZT is set to be 0.5 μm.

blue bars in Fig. 7 are plotted with defocusing amounts that are calculated from the phase difference between designated pattern and Fig. 6(c) which presents the real phase distribution of interferential pattern with 0 μm defocusing amount, while the red bars are plotted, under presupposition that projective objective is aberration-free, with the result that calculated from the phase difference between designated pattern and simulated pattern in Fig. 2(f).

In Fig. 7(a), the PZT performs a step action with 4 μm step length. As we can see, errors tend to decrease as the defocusing amounts decrease, which is in according with the derivation in Section 3 that "The high-frequency fringes in the border of Fig. 3(a) and (d) are more sensitive to the disturbances." Considering the aberration, the errors introduced by the phase unwrapping algorithms and environmental factors may fluctuate around ± 2 μm, while the red bars indicate much larger errors around ± 6 μm, which caused by joint influences of objective aberration, environmental factors and algorithm errors.

When defocusing amount decreases to less than ± 10 μm, another set of interferential patterns, which shape as slightly curved fringes, with 0.5 μm step length is recorded. The Fourier transform based algorithm shows focusing errors fluctuate within ± 0.3 μm (Fig. 7(b)). Specifically, when the wafer is defocused around ideal focal plane within ± 2 μm range, the focusing method achieves a good performance of accuracy at nanometer scale. These high-performance results benefit from the high ultimate resolution of this coaxial focusing system. For an approximate estimation, the ultimate resolution can be derived from Eq. (6) as

$$\alpha_{resolution} = \frac{1}{m \cdot n} \sum_m \sum_n \frac{\Delta\varphi_{spherical} \cdot f^2}{k\left[(10x)^2 + (10y)^2\right]} \tag{8}$$

where $m = 576$ and $n = 768$ are the corresponding row and column pixel numbers of the CCD, and the coefficient 10 is the pixel width. Considering that the phase distribution of the interferential patterns can be extracted with preserved accuracy of better than 0.1 rad ($\Delta \varphi_{spherical}$ varies within ± 0.1 rad at all pixel points), the ultimate resolution $\alpha_{resolution}$ can be figured as 1.78 nm.

Contrasting the extents of red and blue bars, two conclusions can be drawn reasonably. On the one hand, the objective aberration takes main share among all the influential factors that impede the focusing accuracy. On the other hand, the compensation method is very effective in eliminating error caused from aberration.

Except for the high accuracy of the coaxial focusing scheme, another advantageous feature becomes more prominent when a projective objective with higher number aperture (NA) and lower focal length (f) are employed to improve the resolution. In tradition, the "Off-axis" focusing methods used a lower f with shorter distance between wafer and objective causing difficulties to conduct a triangle reflection scheme. Instead, in the coaxial focusing system, a lower f could cause greater phase variation against a fixed defocusing amount α according to Eq. (5). In other words the coaxial focusing way enhances the sensitivity of the whole system.

5. Summary

To summarize, we introduced an interferometric focusing approach to coaxially locate the ideal wafer focal plane in projection lithography; the approach, based on phase unwrapping of designated fringes encoded the defocusing amounts, is possible to achieve sensitivity at nanometer level with consideration of the objective aberration. Analyses indicate that proposed method has obvious superiority in accuracy and adaptability against the traditional methods, particularly when the focal length of projective objective narrows rapidly. Furthermore, coaxial focusing scheme can be preferentially applied to the immersion lithography tools, where the application of the traditional triangle reflection systems is limited with asymmetric liquid distribution.

Acknowledgment

References

[1] K. Tawarayama *et al.,* "Recent progress of EUV full-field exposure tool in Selete," in *Proc. SPIE Adv. Lithogr.*, Mar. 2009, pp. 727 118–727 125.
[2] F. Kahlenberg *et al.,* "Best focus determination: Bridging the gap between optical and physical topography," in *Proc. Adv. Lithogr., Int. Soc. Opt. Photon.*, Mar. 2007, vol. 6520, pp. 65200Z–65208Z.
[3] D. Kim *et al.,* "Focusing and leveling system using position-sensitive detectors for the wafer steppers," in *Proc. Symp. Microlithogr., Int. Soc. Opt. Photon.*, May 1994, vol. 2197, pp. 997–1003.
[4] T. Huang, S. Liu, P. Yi, and T. Shi, "Focusing and leveling system for optical lithography using linear CCD," in *Proc. Int. Conf. Opt. Instrum. Technol.*, Dec. 2008, vol. 7160, pp. 71602X–71608X.
[5] D. C. Flanders and T. M. Lyszczarz, "A precision wide-range optical gap measurement technique," *J. Vac. Sci. Technol. B, Microelectron. Nanom. Struct.*, vol. 1, no. 4, pp. 1196–1199, Oct. 1983.
[6] Y. Oshida, M. Tanaka, T. Tanimoto, and T. Kurosaki, "Chip leveling and focusing with laser interferometry," in *Proc. Microlithogr.*, Jun. 1990, vol. 1264, pp. 244–251.
[7] K. Kato, T. Itoh, and N. Atoda, "A new optical heterodyne alignment and gap detection technique for X-ray steppers," *Microelectron. Eng.*, vol. 23, no. 1, pp. 185–188, Jan. 1994.
[8] R. O. Hunter Jr., B. G. MacDonald, and A. H. Smith, "In situ process control system for steppers," U.S. Patent 5202748, Apr.13, 1993.
[9] W. Yan, Y. Yang, W. Chen, S. Hu, and S. Zhou, "Moiré-based focusing and leveling scheme for optical projection lithography," *Appl. Opt.*, vol. 49, no. 31, pp. 5959–5963, May 2010.
[10] N. Li, W. Wu, and S. Chou, "Sub-20-nm alignment in Nan imprint lithography using Moiré fringes," *Nano Lett.*, vol. 6, no. 11, pp. 2626–2629, Nov. 2006.
[11] E. E. Moon and H. I. Smith, "Nanometer-precision pattern registration for scanning-probe lithographies using interferometric-spatial-phase imaging," *J. Vac. Sci. Technol. B, Microelectron. Nanom. Struct.*, vol. 24, no. 6, pp. 3083–3087, Nov. 2006.
[12] S. Zhou *et al.,* "Moiré-based phase imaging for sensing and adjustment of in-plane twist angle," *IEEE Photon. Technol. Lett.*, vol. 25, no. 18, pp. 1847–1850, Sep. 2013.

[13] Y. Matsui, N. Onoda, S. Nagahara, and T. Uchiyama, "Defect reduction in ArF immersion lithography using particle trap wafers with CVD thin films," *IEEE Trans. Semicond. Manuf.*, vol. 22, no. 4, pp. 438–442, Nov. 2009.

[14] W. Fyen and P. W. Mertens, "An analytical model to describe the efficiency of an immersion rinsing process," *IEEE Trans. Semicond. Manuf.*, vol. 21, no. 4, pp. 661–667, Nov. 2008.

[15] M. Narwaria, W. Lin, I. V. McLoughlin, S. Emmanuel, and L. T. Chia, "Fourier transform-based scalable image quality measure," *IEEE Trans. Image Process.*, vol. 21, no. 8, pp. 3364–3377, Aug. 2012.

[16] M. Servin, J. C. Estrada, and O. Medina, "Fourier transform demodulation of pixilated phase-masked interferograms," *Opt. Exp.*, vol. 18, no. 15, pp. 16 090–16 095, Jul. 2010.

[17] L. R. Watkins, S. M. Tan, and T. H. Barnes, "Determination of interferometer phase distributions by use of wavelets," *Opt. Lett.*, vol. 24, no. 13, pp. 905–907, Jul. 1999.

[18] L. T. Bang, W. Li, M. L. Piao, M. A. Alam, and N. Kim, "Noise reduction in digital hologram using wavelet transforms and smooth filter for three-dimensional display," *IEEE Photon. J.*, vol. 5, no. 3, art. no. 6800414, Jun. 2013.